APPENDIX

A.1 General Experimental Methods

Materials: All solutions were diluted with water obtained from a Millipore deionized (DI) water system, having a resistivity of 18.2 MΩ·cm. Fumasep FAAM-15 and Nafion^{TM} 117 were obtained from Fuel Cell Store. Sulfuric Acid (TraceMetal Grade) and potassium hydroxide (99.99%, semiconductor grade) was were purchased from Fisher. Ammonium hydroxide (28 – 30 %) was purchased from JT Baker and hydrogen peroxide (ACS reagent, 30%) was obtained from Macron. Buffered oxide etchant (6:1 (v/v) 40% NH_4F to 49% HF) was obtained from Transene. Cobalt(II) chloride hexahydrate ($CoCl_2$, >99.9%) and gallium-indium eutectic (GaIn, 99.99%, metals basis) were obtained from Alfa Aesar.

Cleaning: In general Si samples were cleaned in a Radio Corporation of America, RCA, "Standard Clean 1" SC1 bath (5:1:1 $H_2O/NH_4OH/H_2O_2$, 80 °C for >10 min), buffered oxide etchant (10 s for planar samples and 5 min for wire samples at 20 °C), and an RCA "Standard Clean 2" SC2 bath (6:1:1 $H_2O/HCl/H_2O_2$, 70 °C for >10 min) to remove SiO_2, Al_2O_3 and trace metal impurities.

Homojunction preparation: Immediately after cleaning of the samples followed by oxide removal in HF(aq), n^+ doping of silicon chips was performed in a quartz tube under 10 liters per minute N_2 flow at 850°C with two PH-900 PDS wafers (Saint Gobain) serving as the P source. The P_2O_5 glass formed during the doping procedure was removed from the Si surface via buffered oxide etchant for > 60 s.

Preparation of Si Microwire Arrays: Si was degreased with acetone and isopropyl alcohol and was then spin coated at 4000 rpm for 30 s with Shipley 1813 photoresist. A square array of circles was defined using UV exposure through a chrome mask. The pattern

was developed with MF-319 developer, and the resist was hard-baked at 115 °C for 10 min. Al_2O_3 masks, 125 nm in thickness, were deposited via e-beam evaporation at 1 Å·s^{-1} into the exposed hole array and the resist was removed via sonication in Remover-PG (MicroChem) at 50 °C. Si was structured into 30 μm tall microwire arrays via deep reactive ion etching (RIE) in a SF_6/O_2 plasma controlled by an Oxford Plasmalab System 100 at -130 °C. An inductively coupled plasma power of 900 W produced etching rates of 1 μm min^{-1}, while a low capacitively coupled plasma power of 3-7 W minimized sidewall damage and mask removal.

Physical Characterization: Scanning-electron micrographs (SEMs) were obtained with a FEI Nova NanoSEM 450 at an accelerating voltage of 5.0-15.0 kV and a working distance of 5.0 mm using an Everhart-Thornley secondary electron detector.

A.2 Supporting Information for Chapter 2

Materials: 100mm P-type Si <100> wafers with a thickness of 525 μm and resistivity of 10-20 Ω-cm were obtained from Addison Engineering. All chemicals were commercially available and used as received. Sodium hypophosphite monohydrate ($NaPO_2H_2$), boric acid (H_3BO_3, >99.5%), concentrated ammonium hydroxide (NH_4OH, ACS reagent 28%-30%) and potassium hydroxide (KOH, 99.99%) were obtained from Sigma-Aldrich. Buffered oxide etchant (6:1 (v/v) 40% NH_4F to 49% HF) was obtained from Transene Inc. Sodium chloride (NaCl, 99%) was obtained from Macron Chemicals.

A.3 Supporting Information for Chapter 3

Materials: Isopropyl alcohol, acetone, hydrochloric acid (36.5 - 38.0 %), and nitric acid (67 - 70 %, TraceMetal Grade) were purchased from Millipore, and $CuSO_4$ was purchased from Flinn Scientific. K_2SO_4 (99 %), and potassium bicarbonate (99.995 %) were

purchased from Sigma-Aldrich. Methanol was purchased from VWR Chemical. Buffered oxide etchant (6:1 NH_4F/HF) was purchased from Transene. Boron doped, P-type silicon wafers with a resistivity of 10 - 20 Ω·cm were purchased from Addison Engineering. Platinum foil (99.99 %) was purchased from Alfa Aesar, and copper foil (99.999 %) was obtained from Sigma Aldrich. CO_2 (99.999 %, <1.0 ppm Ar+O_2+CO, <1.0 ppm THC, <3.0 ppm H_2O, <5.0 ppm N_2) was purchased from Airgas.

(Photo)electrodepositions of Catalyst: Prior to electrodeposition of Cu, electrodes were rinsed sequentially with acetone, isopropyl alcohol, methanol, and deionized water and then dipped into buffered oxide etchant for 60 s. Electrodepositions were controlled with a BioLogic SP-200 potentiostat. The Cu-plating bath was continuously purged with Ar(g) and contained 0.10 M $CuSO_4$(aq), 5.0 mM H_2SO_4(aq), and 0.10 M K_2SO_4(aq), at a pH of ~3. A saturated calomel electrode (SCE, CH Instruments) was used as a reference and the counter electrode was a high-purity graphite rod (Alfa Aesar, 5N) **(Figure 3.1A)**. The illumination source was an array of narrowband light-emitting diodes (Luxeon Rebel Blue SMD, FWHM 22 nm) with a peak intensity at 465 nm. The illumination wavelength was selected to maximize transmission of light through the colored electrolyte. Cu was deposited potentiostatically at 0.0 V vs. SCE until the desired charge density had passed, normalized to the projected area of the electrode.

Photoelectrochemical CO_2 Reduction Testing: The electrochemical setup was operated in a continuous flow mode. Carbon dioxide was provided to the electrochemical cell at a flow rate of 5 sccm as controlled by an Alicat flow controller. The carbon dioxide stream was supplied as humidified CO_2 with a gas bubbler placed between the cell and flow controller. The exhaust gases went through a liquid trap, then an Alicat flow meter, and

finally to a gas chromatograph (SRI-8610) using a Hayesep D column and a Molsieve 5A column with N_2 as the carrier gas. The gaseous products were detected using a thermal conductivity detector (TCD) and a flame ionization detector (FID) equipped with a methanizer. Quantitative analysis of gaseous products was based on calibrations with several gas standards over many orders of magnitude in concentration. The calibrations were used to calculate the partial current density, *j*, towards products of the CO_2R and hydrogen evolution reaction. To measure liquid products, the electrolyte on the anode and cathode sides of the cell was sampled at the end of the run and was analyzed by high-performance liquid chromatography (HPLC, Thermo Scientific Ultimate 3000). Products were not quantified in Faradaic efficiency calculations because continuous purging of the catholyte with CO_2 expelled accumulated products. Moreover, crossover of products to the anolyte was observed and oxidation at the anode could potentially occur. An Oriel Instruments 75 W Solar Simulator supplied 100 $mW \cdot cm^{-2}$ of AM 1.5 illumination. The light intensity was calibrated using the measured photocurrent at a calibrated (350 to 1100 nm, 1 cm^2) NIST traceable Si photodiode (Thorlabs FDS1010-CAL) mounted within the testing cell prior to the addition of the electrolyte.

Electrochemical measurements of photoelectrochemical CO_2R: A PEEK compression cell was used as the vessel for the measurement with an anode chamber volume of 2 mL and a cathode chamber volume of 4 mL. The anode, cathode electrode and membrane area were each 1 cm^2 as constrained by the design of the compression cell. CO_2 saturated 0.10 M potassium bicarbonate ($KHCO_3$, pH 6.8) was used as the electrolyte. A Pt foil anode was used behind a Selemion anion exchange membrane. A leakless Ag/AgCl electrode was used as a reference. All electrochemical measurements were performed using

a Biologic VSP-300 potentiostat. Scan rates were set to 50 $mV \cdot s^{-1}$. Cu foil (99.999 %, Sigma Aldrich) was mechanically polished (Struers LabPol-5) using 0.050 µm alumina suspension (MasterPrep) and then was electropolished for 5 min in 85% H_3PO_4 at +2.1 V vs. a carbon counter electrode.

Comparison of Catalyst Loadings: The mass loadings of catalyst were compared assuming a Faradaic efficiency of ~100 % towards metal plating. Equation S1 can be used to calculate the mass loading density, M_{cat} ($mg \cdot cm^{-2}$), from the cathodic charge density, $-Q$ ($C \cdot cm^{-2}$) and molar mass of the catalyst. For Cu (m_a = 63.55 $g \cdot cm^{-2}$), M_{cat} was 0.329 and 0.0487 $mg \cdot cm^{-2}$ for $-Q$ = 1 and 0.148 $C \cdot cm^{-2}$, respectively.

$$M_{cat} = \frac{-Qm_a}{nF} \quad \text{(S1)}$$

Explanation of Resistance Measurement and iR_s Correction: The resistance (R_s) was determined by electrochemical impedance spectroscopy (EIS) at the open-circuit potential. During the experiment, iR_s was corrected by 85% and the remaining 15 % was corrected for after the experiment.

Measurements of Pt Crossover during Stability Testing The rate of Pt dissolution in 0.10 M $KHCO_3$(aq) and crossover through Selemion were measured via a galvanostatic experiment at 10 mA using a Pt anode and a graphite cathode. The volumes of the anolyte and catholyte were each 13 mL. ICP-MS measurements confirmed the presence of dissolved Pt in both the anolyte and catholyte.

Predicted *j-E* behavior: Illuminated *j-E* behavior was predicted by shifting the fitted Tafel behavior of the polished Cu foil towards positive potentials by $V_{ph} + b \log_{10}(R_\mu)$. This calculation assumes a comparable microstructured area of Cu islands and Si and similar [H^+(aq)] and [CO_2(aq)] at the surface of the two electrodes. Simulated *j-E* behaviors in

Figure 4b were produced by summing the implicit values for η and V_{ph}, calculated form Equations 1 and 2, as a function of R_μ and b. Arbitrary values for $J_o = 1 \times 10^{-10}$ A cm^{-2} and $a = 1 \times 10^{-7}$ A cm^{-2} were selected; these parameters do not affect the potential shift resulting from a change in R_μ but affect the total V_{ph} and η observed.

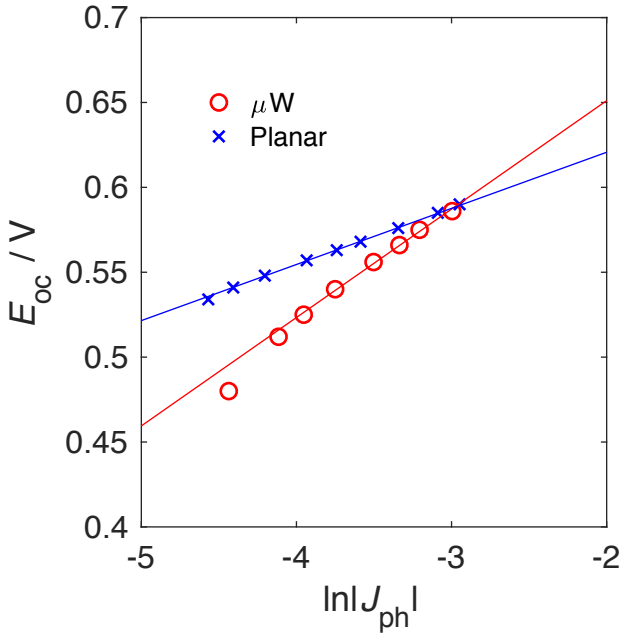

Figure A.3.1: Plot of E_{oc} vs. the ln of the light-limited photocurrent density (A·cm^{-2}) in a Cu plating bath for planar and μW n$^+$p-Si. The illumination source was a narrow band LED with a peak intensity at 630 nm. The illumination wavelength was selected to maximize transmission through the Cu film. The ideality factor was calculated from the slope of the linear fit in range of photocurrent densities relevant to operation under 100 mW·cm-2 of simulated sunlight.

A.4 Supporting Information for Chapter 4

Fabrication of n$^+$p-Si μ–cone photocathodes with Pt: Czochralski-grown p-type Si wafers with a <100> orientation and a resistivity of 0.60-0.80 ohm-cm (Addison Engineering, Inc.) were photolithographically patterned with a square grid of Al_2O_3 circles

that were 3 μm in diameter with a 7 μm pitch. The Al_2O_3 was deposited to a thickness of 200 nm via electron-beam evaporation. The μ–cones were etched from the masked p-Si wafer using an Oxford Dielectric System 100 ICP/RIE following a procedure described previously.[119] A capacitively coupled power of 7 W, and an inductively coupled power of 900 W, was used for etching. Etching was performed in three steps, in which the ratio of SF_6 to O_2 gas was varied stepwise from 70 sccm : 6 sccm to 70 sccm : 7 sccm by increasing the rate of O_2 flow by 0.5 sccm every 30 min. The chamber temperature and pressure were maintained at -130 °C and 10 mTorr, respectively. After etching, samples were cleaned via a modified RCA standard clean 1 (5:1:1 (vol) H_2O:NH_4OH:H_2O_2 at 70 °C) followed by an RCA standard clean 2 (6:1:1 (vol) H_2O:HCl:H_2O_2 at 70 °C). The samples were dipped in HF between the cleaning steps, which also resulted in removal of the Al_2O_3 etch mask. After cleaning, the samples were dipped in ~ 6.5 M HF(aq) for 1 min before thermal P diffusion using a Saint-Gobain PH-900 PDS diffusion-doping source at 850 °C for 15 min under a N_2(g) ambient, to yield an n^+p homojunction. To reduce thermal stresses, the samples were inserted into, and removed from, the doping furnace over the course of 1 min. The Si μ–cones were then heated to 150 °C on a hot plate, and mounting wax (Quickstick 135, South Bay Tech) was melted into the array as a mask. Excess wax was removed by reactive-ion etching using an O_2 plasma at a forward power of 400 W and 300 mTorr operating pressure. The wax was etched until 6-9 μm of the tips of the μ-cones were exposed. The samples were then dipped in ~ 6.5 M HF for ~1 min to remove the native oxide over the Si μ–cones, and Ti and/or Pt were sputtered onto the samples. The reproducible sputtering rate of the system allowed for the thickness to be controlled by the sputtering time and was referenced to a planar control wafer. Metal thicknesses on planar

samples were measured with a DektakXT Profilometer. The samples were then immersed in acetone and sonicated for 15 min to completely remove the wax, resulting in Si μ–cones with metal selectively deposited over the tips of the μ–cones. Samples were cleaved with a carbide scribe into ~10 mm^2 chips and electrodes were fabricated as described above (**A.1**)

Fabrication of p-Si μ-cone photocathodes with Co-P: p-Si μ–cone arrays were fabricated via the above etching and cleaning procedures but were not doped with an n^+ emitter layer. Bottom-facing electrodes were made from the p-Si μ–cones as described in the previous section, and Co/Co-P was photoelectrochemically deposited onto the surface of the p-Si μ–cones using illumination from a narrowband light-emitting diode (LED) (Thorlabs) with an intensity-averaged wavelength of 625 nm. The light intensity at the surface of the sample was ~200 mW cm^{-2}. The Co/Co-P plating bath has been described elsewhere,[26] and was purged vigorously with Ar(g) prior to and during the deposition, with a gas stream in close proximity to the sample to drive local convection.

Fabrication of membrane-embedded p-Si μ-cone photocathodes with Co-P: p-Si μ-cones were embedded in PDMS by spin coating a 10:10:1 (vol) solution of toluene, PDMS elastomer, and curing agent (Dow Sylgard^{TM} 184) at 3000 rpm, leaving the top ~15 μm of the μ-cones exposed. The samples were cured on a hot plate at 150 ^oC for ~ 30 min. The μ-cones were peeled off of the substrate using a razor blade. The flexible polymer membrane was held on its edges sandwiched between Kapton tape and a glass slide, with the back side of the μ-cones facing up. The thickness of the tape ensured that the tips of the μ-cones were not damaged. 500 nm of Au was deposited via electron-beam evaporation onto the backs of the μ-cones. Electrodes were made using these flexible substrates with

Ag ink connecting the Au back contact to a Cu-Sn wire that was fed through 6 mm outer diameter borosilicate glass tubing which was 1 mm thick. Electrodes were fabricated as described above (**A.1**)

Stability testing: Extended stability testing of n^+p-Si/Ti/Pt and p-Si/Co-P μ-cone arrays was performed under nominally identical conditions as those used for photoelectrochemical testing, but with a Pt mesh electrode counter electrode behind a Nafion membrane (Fuel Cell Store). H_2 was bubbled through the electrolyte for the duration of the stability tests to maintain a dissolved concentration of H_2 in equilibrium with 1 atmosphere of H_2(g).

A.5 Supporting Information for Chapter 5

Materials: All chemicals were commercially available and used as received. Sodium hypophosphite monohydrate ($NaPO_2H_2$), boric acid (H_3BO_3, >99.5%), concentrated ammonium hydroxide (NH_4OH, ACS reagent 28%-30%), potassium hydroxide (KOH, 99.99%), and TraceCERT® standards for phosphorus (P 1000 mg/mL) and cobalt (Co 10 mg/mL) were obtained from Sigma-Aldrich. Hydrochloric acid (HCl, ACS grade 36.5-38%) was obtained from Millipore. P-type Si wafers with a resistivity of 10-20 Ω-cm and n-type Si wafers with a resistivity of <0.005 Ω-cm, both with diameters of 100 mm, thicknesses of 525 μm, and <100> orientation, were obtained from Addison Engineering. Fluorine-doped tin oxide (FTO, NSG TEC™ 15) with dimensions of 25 x 100 x 2 mm and a sheet resistance of 14 Ω/□ was obtained from Pilkington. PH-900 PDS diffusion dopant source wafers were purchased from Saint-Gobain.

Metallization: Metallization occurred in an AJA high-vacuum magnetron sputtering unit under a constant flow of Ar at 20 standard cubic centimeters per minute, with the chamber

pressure maintained at 5 mtorr. Ti was deposited via radio-frequency (RF) sputtering at 130 W for 90 s whereas Co was deposited via RF sputtering for 90 s at 150 W.

Fabrication of Electrodes: Silicon electrodes were prepared from individual 5-20 mm^2 chips of metallized n^+-Si and n^+p-Si samples. Ohmic contacts were formed via scratching In-Ga into the backside of the chips. FTO electrodes were prepared from 20-30 mm^2 chips of metallized FTO samples. An adhesive Ag paint having a grain size < 1.0 μm (PELCO, Ted Pella) was used to affix the chips to a Cu-Sn wire that had been fed through 6 mm outer diameter borosilicate glass tubing that was 1 mm thick. Photoactive n^+p-Si chips and FTO samples were sealed onto the end of the glass tubing using an opaque, insulating epoxy (Hysol 9460), whereas n^+-Si samples used for ellipsometry were fixed to the tubing using clear nail polish, which facilitated removal of the samples from the electrode assembly prior to ellipsometric measurements.

(Photo)electrochemical Measurements: (Photo)electrochemical depositions and hydrogen-evolution testing were performed using a Biologic SP-200 potentiostat. Single-compartment glass cells were used for both deposition and testing, with a saturated calomel electrode serving as the reference electrode and a high-purity graphite rod (Alfa Aesar) serving as the counter electrode. The illumination source for depositions was a Thorlabs narrow-band light-emitting diode with a nominal wavelength of 625 nm. The performance of photocathodes for photoelectrochemical hydrogen evolution was measured in H_2-purged 0.50 M H_2SO_4(aq) under 100 mW cm^{-2} of simulated AM1.5 illumination produced by a filtered Hg (Xe) lamp powered at 290 W. *In-situ* transmittance spectra of CoP were recorded using a Biologic VMP3 Multichannel potentiostat connected to a calibrated reference diode (Thorlabs FDS100-CAL) and lock-in amplifier. The illumination source

was a Xe lamp powered at 150 W. The illumination was passed through a monochromator controlled via LabView, and chopped at 10-15 Hz. Light was passed through catalyst films deposited on FTO and collected at the reference diode during electrochemical characterization. Transmittance data were calculated relative to the signal collected through a bare FTO electrode in the cell.

Activation of Electrodeposited CoP: As deposited CoP films were activated via exposure to 10 mL 0.50 M H_2SO_4 (aq) at room temperature under a standard atmosphere. after a specified exposure time. Samples were rinsed with deionized water and dried under a N_2(g) stream to prevent further etching of the film.

Physical characterization: Atomic-force micrographs were recorded with a Bruker Dimension Icon using Peak Force Tapping mode. The Peak Force amplitude and frequency were set to 150 nm and 2 kHz, respectively. For each tapping cycle, a force versus distance curve was recorded by the instrument and a feedback signal was based on the maximum force between the probe and sample. ScanAsyst-Air probes (Bruker) had a nominal tip radius of 2 nm.

Optical characterization: Optical constants were investigated by use of a variable-angle spectroscopic ellipsometer with a rotating analyzer (J.A. Woolam Co., Inc.). Measurements were recorded at an angle of incidence of 70º in 5 nm increments in wavelength over a range from 300 to 1100 nm. A model consisting of a Si substrate, a 1 nm Ti interlayer, and a user-defined "effective medium approximation", EMA, layer composed of CoP and void regions was used to analyze the optical properties of the films as a function of thickness and time immersed in 0.50 M H_2SO_4(aq). A fixed set of optical constants was assumed for the metal fraction of the film, based on the average set of *n* and *k* values measured for CoP

films characterized prior to exposure to 0.50 M H_2SO_4(aq). Only the void fraction and depolarization factor were allowed to vary within an individual set of measurements, whereas the thickness was selected as a constant value that produced the lowest mean-square error (MSE) value across the individual measurements. Allowing for a graded index of refraction within the EMA layer improved the fit (lowered the MSE) but could not be independently verified and was therefore excluded from the model. Allowing the optical properties of the metal fractions to vary would have similarly improved the fit by providing additional degrees of freedom, but no independent measurements could be performed on continuous CoP films after exposure to acid. Hence, in the absence of direct physical data, the optical properties were assumed to be best approximated by those of the "as-deposited" film composition.

Measurement of corrosion products: Dissolved Co and P in 0.50 M H_2SO_4(aq) were quantified via inductively coupled plasma mass spectrometry, ICP-MS, as a function of time spent in acid under galvanostatic control at -10 mA cm^{-2}. The volume of the electrolyte was 50 mL. Samples were recorded by withdrawing 0.500 mL of electrolyte at specified time intervals, which were diluted to a volume of 5.00 mL with deionized water for analysis. To avoid interference from sulfur in the electrolyte, phosphorus was quantified in mass-shift mode by forming a PO^+ species detected at a mass to charge ratio of 47. Concentrations were calculated by comparing ion counts to calibration curves prepared from certified standard solutions.

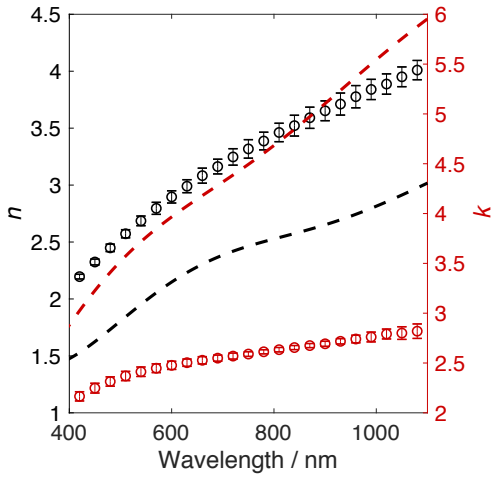

Figure A.5.1: Real (*n*) and imaginary (*k*) components of the complex index of refraction, measured via spectroscopic ellipsometry in air, for as-deposited CoP films deposited to a thickness of 87 ± 12 nm, represented as open circles. Error bars represent one standard deviation between three independent samples. For comparison, *n* and *k* values for an 80 nm Co film are plotted as dashed lines.[137]

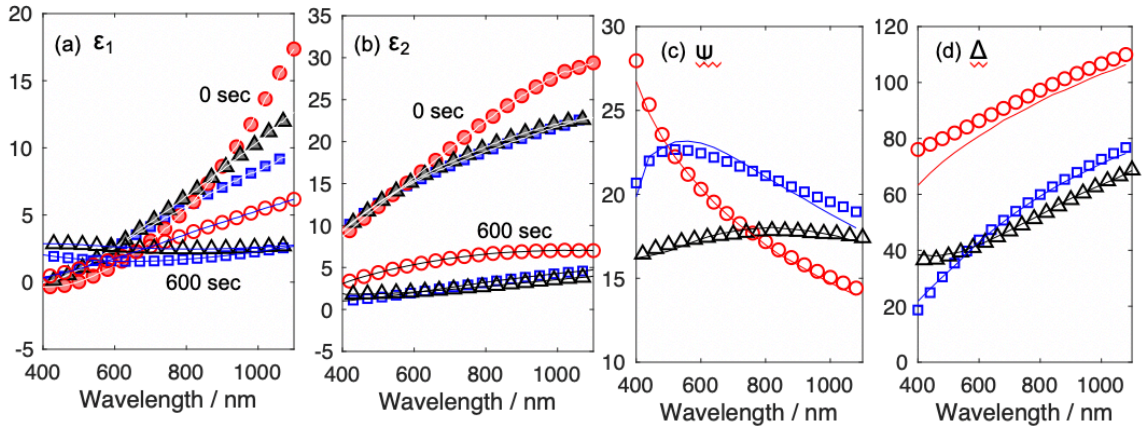

Figure A.5.2: Spectroscopic ellipsometry of n^+-Si/Ti/Co/CoP samples at metal loadings of 400 (red circles), 800 (blue squares) and 1200 (black triangles) mC cm^{-2}. Measured data points are shown as individual markers, simulated data are represented as continuous lines (a) Real components and (b) Imaginary components of the dielectric functions of as deposited CoP films (filled markers) and films activated after 10 minutes of activation in 0.50 M H_2SO_4(aq) (open markers). (c) Comparison of simulated and measured values for parameter Psi. (d) Comparison of simulated and measured values for parameter Delta.

A.6 Supporting Information for Chapter 6

Materials: All chemicals were commercially available and used as received. Fe(II) sulfate heptahydrate (ACS Reagent, >99%), Fe(III) sulfate hydrate (97%) and 1,10-phenanthroline (>99%) were obtained from Sigma-Aldrich, gallium-indium eutectic (GaIn, 99.99%, metals basis) was obtained from Alfa Aesar, and concentrated ammonium hydroxide (NH_4OH, 28%-30%) was obtained from JT Baker. Hydrochloric acid (HCl, ACS grade 36.5-38%), acetone, and isopropyl alcohol were obtained from Millipore. Hydroxylamine sulfate (>98%) was obtained from TCI America. N-type Si wafers with a resistivity < 0.005 Ω-cm and diameters of 100 mm, thicknesses of 525 μm, and <100> orientation, were obtained from Addison Engineering.

Mass transport measurements: The thickness of the diffusion layer was measured via spectrophotometric determination of Fe^{2+} in a Shimadzu Solid Spec 3700 ultraviolet-visible spectrometer, following complexation with 1,10-phenanthroline in 0.50 M H_2SO_4(aq) and mixing the solution with 2.3 mL of 0.2 M sodium acetate (aq) to bring the pH to 4-4.5.[166] The testing cell was set up in a nominally identical manner to the cell used for HER testing, with the addition of 8.80 mL of 0.100 M Fe^{3+}(aq), as Fe(III) sulfate, in 0.50 M H_2SO_4(aq) to the 50 mL electrolyte prior to testing to an initial $C^*_{Fe^{3+}}$= 0.0150 M. The precise concentration of the ferric sulfate stock solution was determined via spectrophotometry, following reduction with hydroxylamine, and assuming a molar extinction for tris(1,10-phenanthroline)iron(II) of 1.10 x 10^4 M^{-1} cm^{-1}.[1,2] A diffusion coefficient of Fe^{3+}(aq) of 5.5 x 10^{-6} cm^2 s^{-1} was assumed in calculating boundary layer thicknesses, assuming planar diffusion (Equation 5.1). The value of $C^*_{Fe^{3+}}$ was adjusted to

be the last recorded concentration of Fe^{2+}(aq), with the concentration of Fe^{2+}(aq) not changing by more than 4% during an individual electrolysis.

Calculations of Growth Coefficients: Radius versus time data for individual bubbles measured via high-speed microscopy were fit to a model for diffusive growth of a gas bubble in a supersaturated medium (**Equation A.6.1**).

$$R(t) = \tilde{b}\left(D_{H_2} t\right)^{1/2} \quad \textbf{(A.6.1)}$$

where $D_{H_2} = 4.5 \times 10^{-5}$ cm^{-2} s^{-1} is the diffusivity of H_2 in solution and $\tilde{b}$ is the dimensionless growth coefficient. When the driving force for bubble growth is small, the effects of advection at the growing surface can be ignored, such that analytical expressions can be derived relating $\tilde{b}$ to $C_{H_2(aq)}$. A self-consistent requirement for neglecting the effects of advection is that the Péclet number, which expresses the ratio of advective and diffusive growth, is < 1. For $\tilde{b} > 1$ this condition does not hold and growth coefficients were thus not directly related to $C_{H_2(aq)}$.

Calculation of Weighted Mean Bubble Diameter: The thickness of the gas bubble layer was variable in time and with position on the electrode surface. The mean bubble diameter, *d*, weighted by the fraction of surface obscured by an individual bubble, was calculated as an approximation of the instantaneous gas bubble layer thickness (**Equation A.6.2**).

$$< d_w >= \frac{\pi}{A} \sum_i^n d_i \times \frac{d_i^2}{4} \quad \textbf{(A.6.2)}$$

Where *A* is the geometric surface area of the electrode, the surface is assumed to be obscured by the projected area of the bubble, and the contact angle is assumed to be large such that the height of the bubble is approximately equal to the diameter.

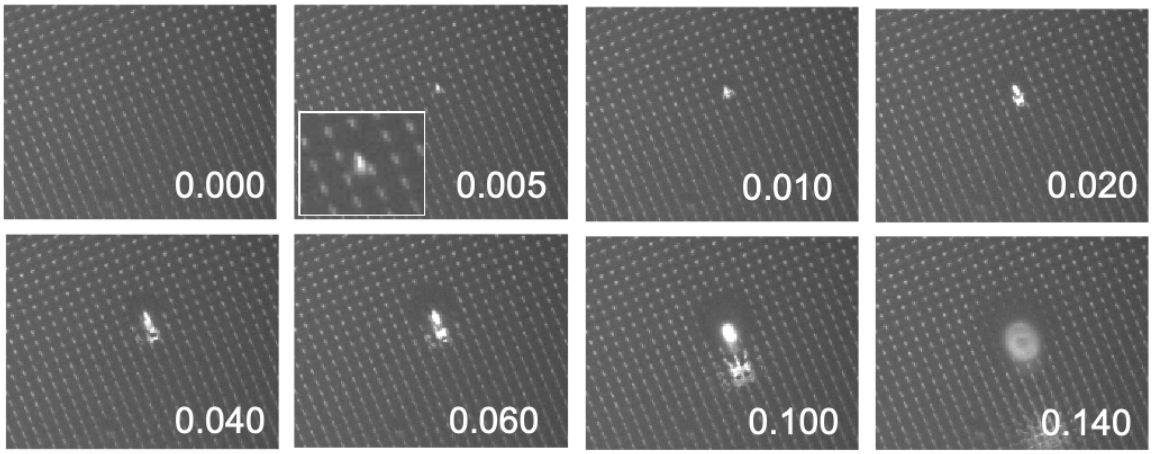

Figure A.6.1: Image sequence at 200 frames s^{-1} and 5-times magnification of an upward-facing µW 6|28 electrode passing 25 mA cm^{-2} of current density for hydrogen evolution. Time stamps are referenced to the first frame and are in seconds. Inset image shows a ~30 µm bubble nucleus forming between microwires. Loss of focus at the bubble surface occurred due to the release from the electrode.

A.7 Supporting Information for Chapter 7

Materials: All chemicals were commercially available and used as received. Conductive Ni and Ag paint were obtained from Ted Pella. Hydrochloric acid (HCl, ACS grade 36.5-38%), acetone, and isopropyl alcohol were obtained from Millipore. Buffered oxide etchant (6:1 (v/v) 40% NH_4F to 49% HF) was obtained from Transene Inc and hydrogen peroxide (H_2O_2, ACS grade 30%) was obtained from Macron Chemicals. Sulfuric acid (H_2SO_4, TraceMetal grade) and potassium hydroxide (KOH, Semiconductor Grade) were obtained from Fisher Scientific. Concentrated ammonium hydroxide (NH_4OH, 28%-30%) was obtained from JT Baker. N-type Si wafers with a resistivity of 0.4 Ω-cm and p-type Si wafers with a resistivity of 10–20 Ω-cm, having diameters of 100 mm, thicknesses of 525 µm, and <100> orientation, were obtained from Addison Engineering. Potassium

hexacyanoferrate(II) trihydrate ($K_4[Fe(CN)_6]\cdot 3H_2O$, >99%) cyanide was obtained from Sigma-Aldrich.

Mass-transport velocity measurements: The current derived from oxidation of $Fe(CN)_6^{4-}$ was calculated based on the change in absorptivity of the electrolyte in the cell before vs after a bulk electrolysis. The electrolyte was not stirred during testing but was vigorously stirred by a magnetically-powered Teflon stir bar prior to sampling the electrolyte. A calibration was performed at a large area Ni coil held potentiostatically at 1.3 V vs RHE. At this potential, the current associated with oxygen evolution was negligible and the current derived from $Fe(CN)_6^{4-}$ oxidation was limited by mass transport. **Figure A.7.2** presents the change in absorptivity at 420 nm as a function of charge passed for a series of such experiments. The concentration of $Fe(CN)_6^{3-}$ in the cell was calculated as Q / nFV where Q is the total charge passed at 1.3 V vs. RHE, n is the number of electrons required for the oxidation (1), F is Faraday's constant (96485 C mol^{-1}) and V is the volume of electrolyte in the cell during oxidation (0.097 L or 0.047 L for cells incorporating the upward-facing and downward-facing electrodes, respectively). The extinction coefficient of 1059 M^{-1} cm^{-1} was calculated from a linear regression of the measured absorbances and calculated concentrations.

Image processing: Images of downward-facing photoelectrodes were processed in MATLAB. The manually defined electrode area restricted the pixel area for data collection, and was used to calibrate the pixels per mm^2 scale at the electrode surface. The location and diameter of bubbles were recorded for each image, and the fractional coverage was calculated relative to the geometric electrode area. Manual quantification of bubbles was supplemented by automatic detection of similarly sized bubbles using a Hough transform.

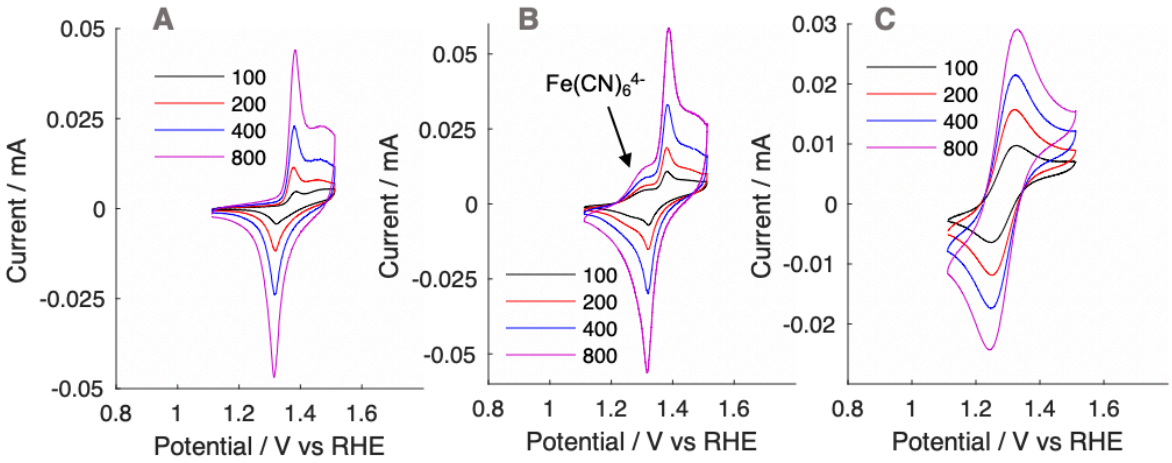

Figure A.7.1: (**A**) Cyclic voltammogram of a polished, 0.5 mm diameter Ni wire embedded in epoxy in 1.0 M KOH(aq). The scan rate is specified in mV s^{-1}. (**B**) Cyclic voltammogram of 10 mM $Fe(CN)_6^{4-}$ in 1.0 M KOH(aq) at a polished, 0.5 mm diameter Ni wire embedded in epoxy. (**C**) Cyclic voltammogram of 10 mM $Fe(CN)_6^{4-}$ in 1.0 M KOH(aq) at a Au wire embedded in borosilicate glass tubing.

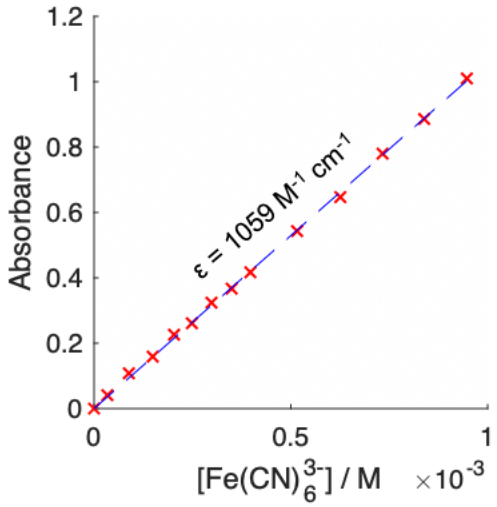

Figure A.7.2: Electrolyte absorbance at 420 nm versus $[Fe(CN)_6^{3-}]$ as measured via the anodic charge passed at a Ni wire in a solution of 10 mM $Fe(CN)_6^{4-}$ in 1.0 M KOH(aq).

REFERENCES

1. Nations, U., Paris Agreement. Change, C., Ed. https://unfccc.int/process-and-meetings/the-paris-agreement/the-paris-agreement, 2015.
2. Sachs, J. D.; Schmidt-Traub, G.; Williams, J., Pathways to Zero Emissions. *Nature Geoscience* **2016,** *9* (11), 799-801.
3. Jenkins, J. D.; Luke, M.; Thernstrom, S., Getting to Zero Carbon Emissions in the Electric Power Sector. *Joule* **2018,** *2* (12), 2498-2510.
4. Lewis, N. S.; Nocera, D. G., Powering the Planet: Chemical Challenges in Solar Energy Utilization. *Proceedings of the National Academy of Sciences* **2006,** *103* (43), 15729-15735.
5. Smits, F. M., History of Silicon Solar Cells. *IEEE Transactions on Electron Devices* **1976,** *23* (7), 640-643.
6. Green, M. A., How Did Solar Cells Get So Cheap? *Joule* **2019,** *3* (3), 631-633.
7. Phillips, S. *Photovoltaics Report*; Fraunhofer Institute for Solar Energy Systems, ISE: 2020.
8. Vartiainen, E.; Masson, G.; Breyer, C.; Moser, D.; Román Medina, E., Impact of Weighted Average Cost of Capital, Capital Expenditure, and Other Parameters on Future Utility-Scale Pv Levelised Cost of Electricity. *Progress in Photovoltaics: Research and Applications* **2020,** *28* (6), 439-453.
9. Davis, S. J.; Lewis, N. S.; Shaner, M.; Aggarwal, S.; Arent, D.; Azevedo, I. L.; Benson, S. M.; Bradley, T.; Brouwer, J.; Chiang, Y.-M., Net-Zero Emissions Energy Systems. *Science* **2018,** *360* (6396).
10. Shaner, M. R.; Davis, S. J.; Lewis, N. S.; Caldeira, K., Geophysical Constraints on the Reliability of Solar and Wind Power in the United States. *Energy & Environmental Science* **2018,** *11* (4), 914-925.
11. Agency, I. E. Countries and Regions. https://www.iea.org/countries.
12. Clack, C. T.; Qvist, S. A.; Apt, J.; Bazilian, M.; Brandt, A. R.; Caldeira, K.; Davis, S. J.; Diakov, V.; Handschy, M. A.; Hines, P. D., Evaluation of a Proposal for Reliable Low-Cost Grid Power with 100% Wind, Water, and Solar. *Proceedings of the National Academy of Sciences* **2017,** *114* (26), 6722-6727.
13. Dowling, J. A.; Rinaldi, K. Z.; Ruggles, T. H.; Davis, S. J.; Yuan, M.; Tong, F.; Lewis, N. S.; Caldeira, K., Role of Long-Duration Energy Storage in Variable Renewable Electricity Systems. *Joule* **2020**.
14. McKone, J. R.; Lewis, N. S.; Gray, H. B., Will Solar-Driven Water-Splitting Devices See the Light of Day? *Chemistry of Materials* **2013,** *26* (1), 407-414.
15. Staffell, I.; Scamman, D.; Abad, A. V.; Balcombe, P.; Dodds, P. E.; Ekins, P.; Shah, N.; Ward, K. R., The Role of Hydrogen and Fuel Cells in the Global Energy System. *Energy & Environmental Science* **2019,** *12* (2), 463-491.
16. Shaner, M. R.; Atwater, H. A.; Lewis, N. S.; McFarland, E. W., A Comparative Technoeconomic Analysis of Renewable Hydrogen Production Using Solar Energy. *Energy & Environmental Science* **2016,** *9*, 2354-2371.
17. Nielander, A. C.; Shaner, M. R.; Papadantonakis, K. M.; Francis, S. A.; Lewis, N. S., A Taxonomy for Solar Fuels Generators. *Energy & Environmental Science* **2015,** *8* (1), 16-25.

18. Ager, J. W.; Shaner, M. R.; Walczak, K. A.; Sharp, I. D.; Ardo, S., Experimental Demonstrations of Spontaneous, Solar-Driven Photoelectrochemical Water Splitting. *Energy & Environmental Science* **2015,** *8* (10), 2811-2824.
19. Lewis, N. S., Developing a Scalable Artificial Photosynthesis Technology through Nanomaterials by Design. *Nature Nanotechnology* **2016,** *11* (12), 1010-1019.
20. Singh, M. R.; Clark, E. L.; Bell, A. T., Effects of Electrolyte, Catalyst, and Membrane Composition and Operating Conditions on the Performance of Solar-Driven Electrochemical Reduction of Carbon Dioxide. *Physical Chemistry Chemical Physics* **2015,** *17* (29), 18924-18936.
21. Khaselev, O.; Turner, J. A., A Monolithic Photovoltaic-Photoelectrochemical Device for Hydrogen Production Via Water Splitting. *Science* **1998,** *280* (5362), 425-427.
22. Vijselaar, W. J.; Perez-Rodriguez, P.; Westerik, P. J.; Tiggelaar, R. M.; Smets, A. H.; Gardeniers, H.; Huskens, J., A Stand-Alone Si-Based Porous Photoelectrochemical Cell. *Advanced Energy Materials* **2019,** *9* (19), 1803548.
23. Shinde, A.; Suram, S. K.; Yan, Q.; Zhou, L.; Singh, A. K.; Yu, J.; Persson, K. A.; Neaton, J. B.; Gregoire, J. M., Discovery of Manganese-Based Solar Fuel Photoanodes Via Integration of Electronic Structure Calculations, Pourbaix Stability Modeling, and High-Throughput Experiments. *ACS Energy Letters* **2017,** *2* (10), 2307-2312.
24. McCrory, C. C.; Jung, S.; Ferrer, I. M.; Chatman, S. M.; Peters, J. C.; Jaramillo, T. F., Benchmarking Hydrogen Evolving Reaction and Oxygen Evolving Reaction Electrocatalysts for Solar Water Splitting Devices. *Journal of the American Chemical Society* **2015,** *137* (13), 4347-57.
25. Bae, D.; Seger, B.; Vesborg, P. C.; Hansen, O.; Chorkendorff, I., Strategies for Stable Water Splitting Via Protected Photoelectrodes. *Chemical Society Reviews* **2017,** *46* (7), 1933-1954.
26. Saadi, F. H.; Carim, A. I.; Verlage, E.; Hemminger, J. C.; Lewis, N. S.; Soriaga, M. P., CoP as an Acid-Stable Active Electrocatalyst for the Hydrogen-Evolution Reaction: Electrochemical Synthesis, Interfacial Characterization and Performance Evaluation. *J. Phys. Chem. C* **2014,** *118* (50), 29294-29300.
27. Ledendecker, M.; Mondschein, J. S.; Kasian, O.; Geiger, S.; Göhl, D.; Schalenbach, M.; Zeradjanin, A.; Cherevko, S.; Schaak, R. E.; Mayrhofer, K., Stability and Activity of Non-Noble-Metal-Based Catalysts toward the Hydrogen Evolution Reaction. *Angewandte Chemie International Edition* **2017,** *56* (33), 9767-9771.
28. Seh, Z. W.; Kibsgaard, J.; Dickens, C. F.; Chorkendorff, I.; Nørskov, J. K.; Jaramillo, T. F., Combining Theory and Experiment in Electrocatalysis: Insights into Materials Design. *Science* **2017,** *355* (6321).
29. Boettcher, S. W.; Warren, E. L.; Putnam, M. C.; Santori, E. A.; Turner-Evans, D.; Kelzenberg, M. D.; Walter, M. G.; McKone, J. R.; Brunschwig, B. S.; Atwater, H. A., Photoelectrochemical Hydrogen Evolution Using Si Microwire Arrays. *Journal of the American Chemical Society* **2011,** *133* (5), 1216-1219.
30. Kelzenberg, M. D.; Boettcher, S. W.; Petykiewicz, J. A.; Turner-Evans, D. B.; Putnam, M. C.; Warren, E. L.; Spurgeon, J. M.; Briggs, R. M.; Lewis, N. S.; Atwater, H. A., Enhanced Absorption and Carrier Collection in Si Wire Arrays for Photovoltaic Applications. *Nature Materials* **2010,** *9*, 239.

31. Ardo, S.; Park, S. H.; Warren, E. L.; Lewis, N. S., Unassisted Solar-Driven Photoelectrosynthetic HI Splitting Using Membrane-Embedded Si Microwire Arrays. *Energy & Environmental Science* **2015,** *8* (5), 1484-1492.
32. Chen, Y.; Sun, K.; Audesirk, H.; Xiang, C.; Lewis, N. S., A Quantitative Analysis of the Efficiency of Solar-Driven Water-Splitting Device Designs Based on Tandem Photoabsorbers Patterned with Islands of Metallic Electrocatalysts. *Energy & Environmental Science* **2015,** *8* (6), 1736-1747.
33. Sun, K.; Moreno-Hernandez, I. A.; Schmidt, W. C.; Zhou, X.; Crompton, J. C.; Liu, R.; Saadi, F. H.; Chen, Y.; Papadantonakis, K. M.; Lewis, N. S., A Comparison of the Chemical, Optical and Electrocatalytic Properties of Water-Oxidation Catalysts for Use in Integrated Solar-Fuel Generators. *Energy & Environmental Science* **2017,** *10* (4), 987-1002.
34. Trotochaud, L.; Mills, T. J.; Boettcher, S. W., An Optocatalytic Model for Semiconductor–Catalyst Water-Splitting Photoelectrodes Based on in Situ Optical Measurements on Operational Catalysts. *The Journal of Physical Chemistry Letters* **2013,** *4* (6), 931-935.
35. Sun, K.; Saadi, F. H.; Lichterman, M. F.; Hale, W. G.; Wang, H.-P.; Zhou, X.; Plymale, N. T.; Omelchenko, S. T.; He, J.-H.; Papadantonakis, K. M., Stable Solar-Driven Oxidation of Water by Semiconducting Photoanodes Protected by Transparent Catalytic Nickel Oxide Films. *Proceedings of the National Academy of Sciences* **2015,** *112* (12), 3612-3617.
36. Zhou, X.; Liu, R.; Sun, K.; Papadantonakis, K. M.; Brunschwig, B. S.; Lewis, N. S., 570 Mv Photovoltage, Stabilized N-Si/CoO_x Heterojunction Photoanodes Fabricated Using Atomic Layer Deposition. *Energy & Environmental Science* **2016,** *9* (3), 892-897.
37. Kayes, B. M.; Atwater, H. A.; Lewis, N. S., Comparison of the Device Physics Principles of Planar and Radial P-N Junction Nanorod Solar Cells. *Journal of Applied Physics* **2005,** *97* (11), 114302.
38. Hochbaum, A. I.; Fan, R.; He, R.; Yang, P., Controlled Growth of Si Nanowire Arrays for Device Integration. *Nano Letters* **2005,** *5* (3), 457-460.
39. Warren, E. L.; McKone, J. R.; Atwater, H. A.; Gray, H. B.; Lewis, N. S., Hydrogen-Evolution Characteristics of Ni–Mo-Coated, Radial Junction, n^+p-Silicon Microwire Array Photocathodes. *Energy & Environmental Science* **2012,** *5* (11), 9653.
40. Shaner, M. R.; McKone, J. R.; Gray, H. B.; Lewis, N. S., Functional Integration of Ni–Mo Electrocatalysts with Si Microwire Array Photocathodes to Simultaneously Achieve High Fill Factors and Light-Limited Photocurrent Densities for Solar-Driven Hydrogen Evolution. *Energy & Environmental Science* **2015,** *8* (10), 2977-2984.
41. Hellstern, T. R.; Benck, J. D.; Kibsgaard, J.; Hahn, C.; Jaramillo, T. F., Engineering Cobalt Phosphide (CoP) Thin Film Catalysts for Enhanced Hydrogen Evolution Activity on Silicon Photocathodes. *Advanced Energy Materials* **2016,** *6* (4).
42. Kempler, P. A.; Gonzalez, M. A.; Papadantonakis, K. M.; Lewis, N. S., Hydrogen Evolution with Minimal Parasitic Light Absorption by Dense Co–P Catalyst Films on Structured P-Si Photocathodes. *ACS Energy Letters* **2018,** *3* (3), 612-617.
43. Yalamanchili, S.; Emmer, H. S.; Fountaine, K. T.; Chen, C. T.; Lewis, N. S.; Atwater, H. A., Enhanced Absorption and <1% Spectrum-and-Angle-Averaged Reflection in Tapered Microwire Arrays. *ACS Photonics* **2016,** *3* (10), 1854-1861.

44. Yalamanchili, S.; Kempler, P. A.; Papadantonakis, K. M.; Atwater, H. A.; Lewis, N. S., Integration of Electrocatalysts with Silicon Microcone Arrays for Minimization of Optical and Overpotential Losses During Sunlight-Driven Hydrogen Evolution. *Sustainable Energy & Fuels* **2019,** *3*, 2227-2236.
45. Saive, R.; Borsuk, A. M.; Emmer, H. S.; Bukowsky, C. R.; Lloyd, J. V.; Yalamanchili, S.; Atwater, H. A., Effectively Transparent Front Contacts for Optoelectronic Devices. *Advanced Optical Materials* **2016,** *4* (10), 1470-1474.
46. Heller, A.; Aspnes, D.; Porter, J.; Sheng, T.; Vadimsky, R., Transparent Metals Preparation and Characterization of Light-Transmitting Platinum Films. *Journal of Physical Chemistry* **1985,** *89* (21), 4444-4452.
47. Bard, A. J.; Faulkner, L. R.; Leddy, J.; Zoski, C. G., *Electrochemical Methods: Fundamentals and Applications*. wiley New York: 1980; Vol. 2.
48. Cheng, W.-H.; Richter, M. H.; May, M. M.; Ohlmann, J.; Lackner, D.; Dimroth, F.; Hannappel, T.; Atwater, H. A.; Lewerenz, H.-J., Monolithic Photoelectrochemical Device for Direct Water Splitting with 19% Efficiency. *ACS Energy Letters* **2018,** *3* (8), 1795-1800.
49. Zhang, X.; Meng, F.; Mao, S.; Ding, Q.; Shearer, M. J.; Faber, M. S.; Chen, J.; Hamers, R. J.; Jin, S., Amorphous MoS_xCl_y Electrocatalyst Supported by Vertical Graphene for Efficient Electrochemical and Photoelectrochemical Hydrogen Generation. *Energy & Environmental Science* **2015,** *8* (3), 862-868.
50. Zhang, H.; Ding, Q.; He, D.; Liu, H.; Liu, W.; Li, Z.; Yang, B.; Zhang, X.; Lei, L.; Jin, S., A P-Si/$NiCoSe_x$ Core/Shell Nanopillar Array Photocathode for Enhanced Photoelectrochemical Hydrogen Production. *Energy & Environmental Science* **2016,** *9* (10), 3113-3119.
51. Ding, Q.; Zhai, J.; Cabán-Acevedo, M.; Shearer, M. J.; Li, L.; Chang, H. C.; Tsai, M. L.; Ma, D.; Zhang, X.; Hamers, R. J., Designing Efficient Solar-Driven Hydrogen Evolution Photocathodes Using Semitransparent MoQ_xCl_y (Q= S, Se) Catalysts on Si Micropyramids. *Advanced Materials* **2015,** *27* (41), 6511-6518.
52. Ding, Q.; Song, B.; Xu, P.; Jin, S., Efficient Electrocatalytic and Photoelectrochemical Hydrogen Generation Using Mos2 and Related Compounds. *Chem* **2016,** *1* (5), 699-726.
53. Kempler, P. A.; Richter, M. H.; Cheng, W.-H.; Brunschwig, B. S.; Lewis, N. S., Si Microwire-Array Photocathodes Decorated with Cu Allow CO_2 Reduction with Minimal Parasitic Absorption of Sunlight. *ACS Energy Letters* **2020**.
54. Vijselaar, W.; Westerik, P.; Veerbeek, J.; Tiggelaar, R. M.; Berenschot, E.; Tas, N. R.; Gardeniers, H.; Huskens, J., Spatial Decoupling of Light Absorption and Catalytic Activity of Ni–Mo-Loaded High-Aspect-Ratio Silicon Microwire Photocathodes. *Nature Energy* **2018,** *3* (3), 185-192.
55. Sun, K.; Ritzert, N. L.; John, J.; Tan, H.; Hale, W. G.; Jiang, J.; Moreno-Hernandez, I.; Papadantonakis, K. M.; Moffat, T. P.; Brunschwig, B. S., Performance and Failure Modes of Si Anodes Patterned with Thin-Film Ni Catalyst Islands for Water Oxidation. *Sustainable Energy & Fuels* **2018,** *2* (5), 983-998.
56. Rossi, R. C.; Lewis, N. S., Investigation of the Size-Scaling Behavior of Spatially Nonuniform Barrier Height Contacts to Semiconductor Surfaces Using Ordered Nanometer-Scale Nickel Arrays on Silicon Electrodes. *J. Phys. Chem. B* **2001,** *105* (49), 12303-12318.

57. Bao, X.-Q.; Cerqueira, M. F.; Alpuim, P.; Liu, L., Silicon Nanowire Arrays Coupled with Cobalt Phosphide Spheres as Low-Cost Photocathodes for Efficient Solar Hydrogen Evolution. *Chemical Communications* **2015,** *51* (53), 10742-10745.
58. Vijselaar, W.; Westerik, P.; Veerbeek, J.; Tiggelaar, R. M.; Berenschot, E.; Tas, N. R.; Gardeniers, H.; Huskens, J., Spatial Decoupling of Light Absorption and Catalytic Activity of Ni–Mo-Loaded High-Aspect-Ratio Silicon Microwire Photocathodes. *Nature Energy* **2018**, 1.
59. Roske, C. W.; Popczun, E. J.; Seger, B.; Read, C. G.; Pedersen, T.; Hansen, O.; Vesborg, P. C. K.; Brunschwig, B. S.; Schaak, R. E.; Chorkendorff, I., et al., Comparison of the Performance of CoP-Coated and Pt-Coated Radial Junction n^+p-Silicon Microwire-Array Photocathodes for the Sunlight-Driven Reduction of Water to H_2(g). *Journal of Physical Chemistry Letters* **2015,** *6* (9), 1679-1683.
60. Shaner, M. R.; McKone, J. R.; Gray, H. B.; Lewis, N. S., Functional Integration of Ni-Mo Electrocatalysts with Si Microwire Array Photocathodes to Simultaneously Achieve High Fill Factors and Light-Limited Photocurrent Densities for Solar-Driven Hydrogen Evolution. *Energy & Environmental Science* **2015,** *8* (10), 2977-2984.
61. Saadi, F. H.; Carim, A. I.; Drisdell, W. S.; Gul, S.; Baricuatro, J. H.; Yano, J.; Soriaga, M. P.; Lewis, N. S., Operando Spectroscopic Analysis of CoP Films Electrocatalyzing the Hydrogen-Evolution Reaction. *Journal of the American Chemical Society* **2017,** *139* (37), 12927-12930.
62. Döscher, H.; Geisz, J. F.; Deutsch, T. G.; Turner, J. A., Sunlight Absorption in Water – Efficiency and Design Implications for Photoelectrochemical Devices. *Energy & Environmental Science* **2014,** *7* (9), 2951-2956.
63. McIntosh, K. R.; Baker-Finch, S. C. In *Opal 2: Rapid Optical Simulation of Silicon Solar Cells*, Photovoltaic Specialists Conference (PVSC), 2012 38th IEEE, IEEE: 2012; pp 000265-000271.
64. Walter, M. G.; Warren, E. L.; McKone, J. R.; Boettcher, S. W.; Mi, Q.; Santori, E. A.; Lewis, N. S., Solar Water Splitting Cells. *Chemical Reviews.* **2010,** *110*, 6446-6473.
65. Coridan, R. H.; Nielander, A. C.; Francis, S. A.; McDowell, M. T.; Dix, V.; Chatman, S. M.; Lewis, N. S., Methods for Comparing the Performance of Energy-Conversion Systems for Use in Solar Fuels and Solar Electricity Generation. *Energy & Environmental Science* **2015,** *8*, 2886-2901.
66. Zhang, H.; Li, A.; Wang, Z.; Ma, W.; Li, D.; Zong, X.; Li, C., Decorating Mesoporous Silicon with Amorphous Metal–Phosphorous-Derived Nanocatalysts Towards Enhanced Photoelectrochemical Water Reduction. *Journal of Materials Chemistry A* **2016,** *4* (39), 14960-14967.
67. Fukami, K.; Kobayashi, K.; Matsumoto, T.; Kawamura, Y. L.; Sakka, T.; Ogata, Y. H., Electrodeposition of Noble Metals into Ordered Macropores in P-Type Silicon. *Journal of The Electrochemical Society* **2008,** *155* (6), D443.
68. Dasog, M.; Carim, A. I.; Yalamanchili, S.; Atwater, H. A.; Lewis, N. S., Profiling Photoinduced Carrier Generation in Semiconductor Microwire Arrays Via Photoelectrochemical Metal Deposition. *Nano Lett.* **2016,** *16*, 5015-5021.
69. Oh, J.; Deutsch, T. G.; Yuan, H.-C.; Branz, H. M., Nanoporous Black Silicon Photocathode for H_2 Production by Photoelectrochemical Water Splitting. *Energy & Environmental Science* **2011,** *4* (5), 1690.

70. Hori, Y.; Murata, A.; Kikuchi, K.; Suzuki, S., Electrochemical Reduction of Carbon Dioxides to Carbon Monoxide at a Gold Electrode in Aqueous Potassium Hydrogen Carbonate. *Journal of the Chemical Society, Chemical Communications* **1987,** (10), 728-729.
71. Saberi Safaei, T.; Mepham, A.; Zheng, X.; Pang, Y.; Dinh, C.-T.; Liu, M.; Sinton, D.; Kelley, S. O.; Sargent, E. H., High-Density Nanosharp Microstructures Enable Efficient CO_2 Electroreduction. *Nano Letters* **2016,** *16* (11), 7224-7228.
72. Hori, Y.; Murata, A.; Takahashi, R., Formation of Hydrocarbons in the Electrochemical Reduction of Carbon Dioxide at a Copper Electrode in Aqueous Solution. *Journal of the Chemical Society, Faraday Transactions 1: Physical Chemistry in Condensed Phases* **1989,** *85* (8), 2309-2326.
73. Kuhl, K. P.; Cave, E. R.; Abram, D. N.; Jaramillo, T. F., New Insights into the Electrochemical Reduction of Carbon Dioxide on Metallic Copper Surfaces. *Energy & Environmental Science* **2012,** *5* (5), 7050-7059.
74. Kumaravel, V.; Bartlett, J.; Pillai, S. C., Photoelectrochemical Conversion of Carbon Dioxide (CO_2) into Fuels and Value-Added Products. *ACS Energy Letters* **2020**.
75. Karamad, M.; Tripkovic, V.; Rossmeisl, J., Intermetallic Alloys as CO Electroreduction Catalysts—Role of Isolated Active Sites. *ACS Catalysis* **2014,** *4* (7), 2268-2273.
76. Kortlever, R.; Peters, I.; Balemans, C.; Kas, R.; Kwon, Y.; Mul, G.; Koper, M. T., Palladium-Gold Catalyst for the Electrochemical Reduction of CO_2 to C1-C5 Hydrocarbons. *Chemical Communications* **2016,** *52* (67), 10229-32.
77. Torelli, D. A.; Francis, S. A.; Crompton, J. C.; Javier, A.; Thompson, J. R.; Brunschwig, B. S.; Soriaga, M. P.; Lewis, N. S., Nickel–Gallium-Catalyzed Electrochemical Reduction of CO_2 to Highly Reduced Products at Low Overpotentials. *ACS Catalysis* **2016,** *6* (3), 2100-2104.
78. Wang, L.; Nitopi, S.; Wong, A. B.; Snider, J. L.; Nielander, A. C.; Morales-Guio, C. G.; Orazov, M.; Higgins, D. C.; Hahn, C.; Jaramillo, T. F., Electrochemically Converting Carbon Monoxide to Liquid Fuels by Directing Selectivity with Electrode Surface Area. *Nature Catalysis* **2019,** *2* (8), 702-708.
79. Kumar, B.; Atla, V.; Brian, J. P.; Kumari, S.; Nguyen, T. Q.; Sunkara, M.; Spurgeon, J. M., Reduced SnO_2 Porous Nanowires with a High Density of Grain Boundaries as Catalysts for Efficient Electrochemical CO_2-into-HCOOH Conversion. *Angewandte Chemie International Edition* **2017,** *56* (13), 3645-3649.
80. Hu, Y.; Chen, F.; Ding, P.; Yang, H.; Chen, J.; Zha, C.; Li, Y., Designing Effective Si/Ag Interface Via Controlled Chemical Etching for Photoelectrochemical CO_2 Reduction. *Journal of Materials Chemistry A* **2018,** *6* (44), 21906-21912.
81. Kong, Q.; Kim, D.; Liu, C.; Yu, Y.; Su, Y.; Li, Y.; Yang, P., Directed Assembly of Nanoparticle Catalysts on Nanowire Photoelectrodes for Photoelectrochemical CO_2 Reduction. *Nano Letters* **2016,** *16* (9), 5675-5680.
82. Hinogami, R.; Mori, T.; Yae, S.; Nakato, Y., Efficient Photoelectrochemical Reduction of Carbon Dioxide on a P-Type Silicon (P-Si) Electrode Modified with Very Small Copper Particles. *Chemistry letters* **1994,** *23* (9), 1725-1728.
83. Cottineau, T.; Morin, M.; Bélanger, D., Modification of P-Type Silicon for the Photoelectrochemical Reduction of CO_2. *ECS Transactions* **2009,** *19* (35), 1-7.

84. Gurudayal; Beeman, J. W.; Bullock, J.; Wang, H.; Eichhorn, J.; Towle, C.; Javey, A.; Toma, F. M.; Mathews, N.; Ager, J. W., Si Photocathode with Ag-Supported Dendritic Cu Catalyst for CO_2 Reduction. *Energy & Environmental Science* **2019,** *12* (3), 1068-1077.
85. Kim, J.; Summers, D.; Frese Jr, K., Reduction of CO_2 and CO to Methane on Cu Foil Electrodes. *Journal of Electroanalytical Chemistry and Interfacial Electrochemistry* **1988,** *245* (1-2), 223-244.
86. Valkonen, E.; Karlsson, B.; Ribbing, C., Solar Optical Properties of Thin Films of Cu, Ag, Au, Cr, Fe, Co, Ni and Al. *Solar Energy* **1984,** *32* (2), 211-222.
87. Hellstern, T. R.; Nielander, A. C.; Chakthranont, P.; King, L. A.; Willis, J. J.; Xu, S.; MacIsaac, C.; Hahn, C.; Bent, S. F.; Prinz, F. B., Nanostructuring Strategies to Increase the Photoelectrochemical Water Splitting Activity of Silicon Photocathodes. *ACS Applied Nano Materials* **2019,** *2* (1), 6-11.
88. Kuhl, K. P.; Hatsukade, T.; Cave, E. R.; Abram, D. N.; Kibsgaard, J.; Jaramillo, T. F., Electrocatalytic Conversion of Carbon Dioxide to Methane and Methanol on Transition Metal Surfaces. *Journal of the American Chemical Society* **2014,** *136* (40), 14107-14113.
89. Dinh, C.-T.; García de Arquer, F. P.; Sinton, D.; Sargent, E. H., High Rate, Selective, and Stable Electroreduction of CO_2 to CO in Basic and Neutral Media. *ACS Energy Letters* **2018,** *3* (11), 2835-2840.
90. Dinh, C.-T.; Burdyny, T.; Kibria, M. G.; Seifitokaldani, A.; Gabardo, C. M.; de Arquer, F. P. G.; Kiani, A.; Edwards, J. P.; De Luna, P.; Bushuyev, O. S., CO_2 Electroreduction to Ethylene Via Hydroxide-Mediated Copper Catalysis at an Abrupt Interface. *Science* **2018,** *360* (6390), 783-787.
91. Schreier, M.; Héroguel, F.; Steier, L.; Ahmad, S.; Luterbacher, J. S.; Mayer, M. T.; Luo, J.; Grätzel, M., Solar Conversion of CO_2 to CO Using Earth-Abundant Electrocatalysts Prepared by Atomic Layer Modification of Cuo. *Nature Energy* **2017,** *2* (7), 17087.
92. Gurudayal, G.; Bullock, J.; Srankó, D. F.; Towle, C. M.; Lum, Y.; Hettick, M.; Scott, M. C.; Javey, A.; Ager, J., Efficient Solar-Driven Electrochemical CO_2 Reduction to Hydrocarbons and Oxygenates. *Energy & Environmental Science* **2017,** *10* (10), 2222-2230.
93. Vijselaar, W.; Tiggelaar, R. M.; Gardeniers, H.; Huskens, J., Efficient and Stable Silicon Microwire Photocathodes with a Nickel Silicide Interlayer for Operation in Strongly Alkaline Solutions. *ACS Energy Letters* **2018,** *3* (5), 1086-1092.
94. Hall, A. S.; Yoon, Y.; Wuttig, A.; Surendranath, Y., Mesostructure-Induced Selectivity in CO_2 Reduction Catalysis. *Journal of the American Chemical Society* **2015,** *137* (47), 14834-14837.
95. Welch, A. J.; DuChene, J. S.; Tagliabue, G.; Davoyan, A.; Cheng, W.-H.; Atwater, H. A., Nanoporous Gold as a Highly Selective and Active Carbon Dioxide Reduction Catalyst. *ACS Applied Energy Materials* **2018,** *2* (1), 164-170.
96. Chen, Y.; Lewis, N. S.; Xiang, C., Operational Constraints and Strategies for Systems to Effect the Sustainable, Solar-Driven Reduction of Atmospheric CO_2. *Energy & Environmental Science* **2015,** *8* (12), 3663-3674.
97. McIntosh, K. R.; Baker-Finch, S. C. In *Opal 2: Rapid Optical Simulation of Silicon Solar Cells*, 2012 38th IEEE Photovoltaic Specialists Conference, 3-8 June 2012; 2012; pp 000265-000271.

98. Rühle, S., Tabulated Values of the Shockley–Queisser Limit for Single Junction Solar Cells. *Solar Energy* **2016,** *130*, 139-147.
99. Cho, S. J.; An, T.; Lim, G., Three-Dimensionally Designed Anti-Reflective Silicon Surfaces for Perfect Absorption of Light. *Chemical Communications* **2014,** *50* (99), 15710-15713.
100. Liu, X.; Coxon, P. R.; Peters, M.; Hoex, B.; Cole, J. M.; Fray, D. J., Black Silicon: Fabrication Methods, Properties and Solar Energy Applications. *Energy & Environmental Science* **2014,** *7* (10), 3223-3263.
101. Yalamanchili, S.; Emmer, H. S.; Lewis, N. S.; Atwater, H. A. In *Highly Absorbing and High Lifetime Tapered Silicon Microwire Arrays as an Alternative for Thin Film Crystalline Silicon Solar Cells*, 2016 IEEE 43rd Photovoltaic Specialists Conference (PVSC), 5-10 June 2016; 2016; pp 2999-3003.
102. Vázquez-Guardado, A.; Boroumand, J.; Franklin, D.; Chanda, D., Broadband Angle-Independent Antireflection Coatings on Nanostructured Light Trapping Solar Cells. *Physical Review Materials* **2018,** *2* (3), 035201.
103. Wang, H.-P.; Sun, K.; Noh, S. Y.; Kargar, A.; Tsai, M.-L.; Huang, M.-Y.; Wang, D.; He, J.-H., High-Performance a-Si/C-Si Heterojunction Photoelectrodes for Photoelectrochemical Oxygen and Hydrogen Evolution. *Nano Letters* **2015,** *15* (5), 2817-2824.
104. Roske, C. W.; Popczun, E. J.; Seger, B.; Read, C. G.; Pedersen, T.; Hansen, O.; Vesborg, P. C. K.; Brunschwig, B. S.; Schaak, R. E.; Chorkendorff, I., et al., Comparison of the Performance of CoP-Coated and Pt-Coated Radial Junction n^+p-Silicon Microwire-Array Photocathodes for the Sunlight-Driven Reduction of Water to H_2(g). *Journal of Physical Chemistry Letters* **2015,** *6* (9), 1679-1683.
105. Chen, Z.; Ye, S.; Wilson, A. R.; Ha, Y.-C.; Wiley, B. J., Optically Transparent Hydrogen Evolution Catalysts Made from Networks of Copper–Platinum Core–Shell Nanowires. *Energy & Environmental Science* **2014,** *7* (4), 1461-1467.
106. Chen, Y.; Sun, K.; Audesirk, H.; Xiang, C.; Lewis, N. S., A Quantitative Analysis of the Efficiency of Solar-Driven Water-Splitting Device Designs Based on Tandem Photoabsorbers Patterned with Islands of Metallic Electrocatalysts. *Energy & Environmental Science.* **2015,** *8*, 1736-1747.
107. Cabán-Acevedo, M.; Stone, M. L.; Schmidt, J. R.; Thomas, J. G.; Ding, Q.; Chang, H.-C.; Tsai, M.-L.; He, J.-H.; Jin, S., Efficient Hydrogen Evolution Catalysis Using Ternary Pyrite-Type Cobalt Phosphosulphide. *Nature Materials* **2015,** *14*, 1245.
108. Bao, X.-Q.; Fatima Cerqueira, M.; Alpuim, P.; Liu, L., Silicon Nanowire Arrays Coupled with Cobalt Phosphide Spheres as Low-Cost Photocathodes for Efficient Solar Hydrogen Evolution. *Chemical Communications* **2015,** *51* (53), 10742-10745.
109. Dai, P.; Xie, J.; Mayer, M. T.; Yang, X.; Zhan, J.; Wang, D., Solar Hydrogen Generation by Silicon Nanowires Modified with Platinum Nanoparticle Catalysts by Atomic Layer Deposition. *Angewandte Chemie International Edition* **2013,** *52* (42), 11119-11123.
110. Oh, I.; Kye, J.; Hwang, S., Enhanced Photoelectrochemical Hydrogen Production from Silicon Nanowire Array Photocathode. *Nano Letters* **2012,** *12* (1), 298-302.
111. Yablonovitch, E., Statistical Ray Optics. *J. Opt. Soc. Am.* **1982,** *72* (7), 899-907.

112. Sainiemi, L.; Jokinen, V.; Shah, A.; Shpak, M.; Aura, S.; Suvanto, P.; Franssila, S., Non-Reflecting Silicon and Polymer Surfaces by Plasma Etching and Replication. *Advanced Materials* **2011,** *23* (1), 122-126.
113. Fountaine, K. T.; Kendall, C. G.; Atwater, H. A., Near-Unity Broadband Absorption Designs for Semiconducting Nanowire Arrays Via Localized Radial Mode Excitation. *Opt. Express* **2014,** *22* (S3), A930-A940.
114. Fountaine, K. T.; Cheng, W.-H.; Bukowsky, C. R.; Atwater, H. A., Near-Unity Unselective Absorption in Sparse Inp Nanowire Arrays. *ACS Photonics* **2016,** *3* (10), 1826-1832.
115. Coridan, R. H.; Nielander, A. C.; Francis, S. A.; McDowell, M. T.; Dix, V.; Chatman, S. M.; Lewis, N. S., Methods for Comparing the Performance of Energy-Conversion Systems for Use in Solar Fuels and Solar Electricity Generation. *Energy & Environmental Science* **2015,** *8* (10), 2886-2901.
116. Mialhe, P.; Charles, J. P.; Khoury, A.; Bordure, G., The Diode Quality Factor of Solar Cells under Illumination. *Journal of Physics D: Applied Physics* **1986,** *19* (3), 483.
117. Yalamanchili, S.; Lewis, N. S.; Atwater, H. A. In *Role of Doping Dependent Radiative and Non-Radiative Recombination in Determining the Limiting Efficiencies of Silicon Solar Cells*, 2018 IEEE 7th World Conference on Photovoltaic Energy Conversion (WCPEC) (A Joint Conference of 45th IEEE PVSC, 28th PVSEC & 34th EU PVSEC), 10-15 June 2018; 2018; pp 3223-3226.
118. Min, B.; Wagner, H.; Dastgheib-Shirazi, A.; Kimmerle, A.; Kurz, H.; Altermatt, P. P., Heavily Doped Si:P Emitters of Crystalline Si Solar Cells: Recombination Due to Phosphorus Precipitation. *Physica Status Solidi RRL: Rapid Research Letters* **2014,** *8* (8), 680-684.
119. Saive, R.; Bukowsky, C. R.; Yalamanchili, S.; Boccard, M.; Saenz, T.; Borsuk, A. M.; Holman, Z.; Atwater, H. A. In *Effectively Transparent Contacts (Etcs) for Solar Cells*, 2016 IEEE 43rd Photovoltaic Specialists Conference (PVSC), 5-10 June 2016; 2016; pp 3612-3615.
120. Saive, R.; Boccard, M.; Saenz, T.; Yalamanchili, S.; Bukowsky, C. R.; Jahelka, P.; Yu, Z. J.; Shi, J.; Holman, Z.; Atwater, H. A., Silicon Heterojunction Solar Cells with Effectively Transparent Front Contacts. *Sustainable Energy & Fuels* **2017,** *1* (3), 593-598.
121. Turner-Evans, D. B.; Emmer, H.; Chen, C. T.; Atwater, H. A., Flexible, Transparent Contacts for Inorganic Nanostructures and Thin Films. *Advanced Materials* **2013,** *25* (29), 4018-4022.
122. Dasog, M.; Carim, A. I.; Yalamanchili, S.; Atwater, H. A.; Lewis, N. S., Profiling Photoinduced Carrier Generation in Semiconductor Microwire Arrays Via Photoelectrochemical Metal Deposition. *Nano Lett.* **2016,** *16* (8), 5015-5021.
123. Spurgeon, J. M.; Plass, K. E.; Kayes, B. M.; Brunschwig, B. S.; Atwater, H. A.; Lewis, N. S., Repeated Epitaxial Growth and Transfer of Arrays of Patterned, Vertically Aligned, Crystalline Si Wires from a Single Si (111) Substrate. *Applied Physics Letters* **2008,** *93* (3), 032112.
124. Shaner, M. R.; Fountaine, K. T.; Ardo, S.; Coridan, R. H.; Atwater, H. A.; Lewis, N. S., Photoelectrochemistry of Core–Shell Tandem Junction N–P^+-Si/N-WO_3 Microwire Array Photoelectrodes. *Energy & Environmental Science* **2014,** *7* (2), 779-790.

125. Shaner, M. R.; McDowell, M. T.; Pien, A.; Atwater, H. A.; Lewis, N. S., Si/Tio$_2$ Tandem-Junction Microwire Arrays for Unassisted Solar-Driven Water Splitting. *Journal of The Electrochemical Society* **2016,** *163* (5), H261-H264.
126. Verlage, E.; Hu, S.; Liu, R.; Jones, R. J.; Sun, K.; Xiang, C.; Lewis, N. S.; Atwater, H. A., A Monolithically Integrated, Intrinsically Safe, 10% Efficient, Solar-Driven Water-Splitting System Based on Active, Stable Earth-Abundant Electrocatalysts in Conjunction with Tandem III–V Light Absorbers Protected by Amorphous TiO_2 Films. *Energy & Environmental Science* **2015,** *8* (11), 3166-3172.
127. Kang, D.; Young, J. L.; Lim, H.; Klein, W. E.; Chen, H.; Xi, Y.; Gai, B.; Deutsch, T. G.; Yoon, J., Printed Assemblies of Gaas Photoelectrodes with Decoupled Optical and Reactive Interfaces for Unassisted Solar Water Splitting. *Nature Energy* **2017,** *2* (5), 17043.
128. Degani, Y.; Sheng, T.; Heller, A.; Aspnes, D.; Studna, A.; Porter, J., "Transparent" Metals: Preparation and Characterization of Light-Transmitting Palladium, Rhodium, and Rhenium Films. *Journal of Electroanalytical Chemistry and Interfacial Electrochemistry* **1987,** *228* (1-2), 167-178.
129. Heller, A.; Aharon-Shalom, E.; Bonner, W.; Miller, B., Hydrogen-Evolving Semiconductor Photocathodes: Nature of the Junction and Function of the Platinum Group Metal Catalyst. *Journal of the American Chemical Society* **1982,** *104* (25), 6942-6948.
130. Aspnes, D.; Heller, A.; Porter, J., Microstructurally Engineered, Optically Transmissive, Electrically Conductive Metal Films. *Journal of Applied Physics* **1986,** *60* (9), 3028-3034.
131. McEnaney, J. M.; Crompton, J. C.; Callejas, J. F.; Popczun, E. J.; Read, C. G.; Lewis, N. S.; Schaak, R. E., Electrocatalytic Hydrogen Evolution Using Amorphous Tungsten Phosphide Nanoparticles. *Chemical Communications* **2014,** *50* (75), 11026-11028.
132. Popczun, E. J.; McKone, J. R.; Read, C. G.; Biacchi, A. J.; Wiltrout, A. M.; Lewis, N. S.; Schaak, R. E., Nanostructured Nickel Phosphide as an Electrocatalyst for the Hydrogen Evolution Reaction. *Journal of the American Chemical Society* **2013,** *135* (25), 9267-9270.
133. Popczun, E. J.; Read, C. G.; Roske, C. W.; Lewis, N. S.; Schaak, R. E., Highly Active Electrocatalysis of the Hydrogen Evolution Reaction by Cobalt Phosphide Nanoparticles. *Angew. Chem. Int. Ed.* **2014,** *53* (21), 5427-5430.
134. Kibsgaard, J.; Tsai, C.; Chan, K.; Benck, J. D.; Nørskov, J. K.; Abild-Pedersen, F.; Jaramillo, T. F., Designing an Improved Transition Metal Phosphide Catalyst for Hydrogen Evolution Using Experimental and Theoretical Trends. *Energy & Environmental Science* **2015,** *8* (10), 3022-3029.
135. Stern, L.-A.; Liardet, L.; Mayer, M. T.; Morales-Guio, C. G.; Grätzel, M.; Hu, X., Photoelectrochemical Deposition of CoP on Cuprous Oxide Photocathodes for Solar Hydrogen Production. *Electrochimica Acta* **2017,** *235*, 311-316.
136. Aspnes, D. E., Optical Properties of Thin Films. *Thin Solid Films* **1982,** *89* (3), 249-262.
137. Palik, E. D., *Handbook of Optical Constants of Solids*. Academic press: 1998; Vol. 3.
138. Sihvola, A. H.; Kong, J. A., Effective Permittivity of Dielectric Mixtures. *IEEE Transactions on Geoscience and Remote Sensing* **1988,** *26* (4), 420-429.

139. Izhar, S.; Nagai, M., Transition Metal Phosphide Catalysts for Hydrogen Oxidation Reaction. *Catalysis Today* **2009,** *146* (1-2), 172-176.
140. Jin, S., Are Metal Chalcogenides, Nitrides, and Phosphides Oxygen Evolution Catalysts or Bifunctional Catalysts? *ACS Energy Letters* **2017,** *2* (8), 1937-1938.
141. Stern, L.-A.; Feng, L.; Song, F.; Hu, X., Ni_2p as a Janus Catalyst for Water Splitting: The Oxygen Evolution Activity of Ni_2P Nanoparticles. *Energy & Environmental Science* **2015,** *8* (8), 2347-2351.
142. Peñas, P.; van der Linde, P.; Vijselaar, W.; van der Meer, D.; Lohse, D.; Huskens, J.; Gardeniers, H.; Modestino, M. A.; Rivas, D. F., Decoupling Gas Evolution from Water-Splitting Electrodes. *Journal of The Electrochemical Society* **2019,** *166* (15), H769-H776.
143. Kocha, S. S.; Montgomery, D.; Peterson, M. W.; Turner, J. A., Photoelectrochemical Decomposition of Water Utilizing Monolithic Tandem Cells. *Solar Energy Materials and Solar Cells* **1998,** *52* (3-4), 389-397.
144. Davis, G. E., Scattering of Light by an Air Bubble in Water. *JOSA* **1955,** *45* (7), 572-581.
145. Dorfi, A. E.; West, A. C.; Esposito, D. V., Quantifying Losses in Photoelectrode Performance Due to Single Hydrogen Bubbles. *The Journal of Physical Chemistry C* **2017,** *121* (48), 26587-26597.
146. Leenheer, A. J.; Atwater, H. A., Water-Splitting Photoelectrolysis Reaction Rate via Microscopic Imaging of Evolved Oxygen Bubbles. *Journal of The Electrochemical Society* **2010,** *157* (9), B1290.
147. Holmes-Gentle, I.; Bedoya-Lora, F.; Alhersh, F.; Hellgardt, K., Optical Losses at Gas Evolving Photoelectrodes: Implications for Photoelectrochemical Water Splitting. *The Journal of Physical Chemistry C* **2018,** *123* (1), 17-28.
148. Kern, W., The Evolution of Silicon Wafer Cleaning Technology. *Journal of the Electrochemical Society* **1990,** *137* (6), 1887.
149. Osseo-Asare, K.; Wei, D.; Mishra, K. K., Dissolution Windows for Wet Chemical Processing of Silicon and Silicon Dioxide: Potential-Ph Diagrams for the Si-F-H_2O System. *Journal of the Electrochemical Society* **1996,** *143* (2), 749.
150. Hu, S.; Shaner, M. R.; Beardslee, J. A.; Lichterman, M.; Brunschwig, B. S.; Lewis, N. S., Amorphous TiO_2 Coatings Stabilize Si, Gaas, and Gap Photoanodes for Efficient Water Oxidation. *Science* **2014,** *344* (6187), 1005-1009.
151. Kempler, P. A.; Coridan, R. H.; Lewis, N. S., Effects of Bubbles on the Electrochemical Behavior of Hydrogen-Evolving Si Microwire Arrays Oriented against Gravity. *Energy & Environmental Science* **2020,** *13*, 1808-1817.
152. Fernandez, D.; Maurer, P.; Martine, M.; Coey, J.; Möbius, M. E., Bubble Formation at a Gas-Evolving Microelectrode. *Langmuir* **2014,** *30* (43), 13065-13074.
153. Janssen, L.; Hoogland, J., The Effect of Electrolytically Evolved Gas Bubbles on the Thickness of the Diffusion Layer—II. *Electrochimica Acta* **1973,** *18* (8), 543-550.
154. Vogt, H.; Stephan, K., Local Microprocesses at Gas-Evolving Electrodes and Their Influence on Mass Transfer. *Electrochimica Acta* **2015,** *155*, 348-356.
155. Peñas, P.; van der Linde, P.; Vijselaar, W.; van der Meer, D.; Lohse, D.; Huskens, J.; Gardeniers, H.; Modestino, M. A.; Rivas, D. F., Decoupling Gas Evolution from Water-Splitting Electrodes. *Journal of The Electrochemical Society* **2019,** *166* (15), H769.

156. Trotochaud, L.; Young, S. L.; Ranney, J. K.; Boettcher, S. W., Nickel–Iron Oxyhydroxide Oxygen-Evolution Electrocatalysts: The Role of Intentional and Incidental Iron Incorporation. *Journal of the American Chemical Society* **2014,** *136* (18), 6744-6753.
157. Smith, T., The Hydrophilic Nature of a Clean Gold Surface. *Journal of Colloid and Interface Science* **1980,** *75* (1), 51-55.
158. Erb, R. A., Wettability of Metals under Continuous Condensing Conditions. *The Journal of Physical Chemistry* **1965,** *69* (4), 1306-1309.
159. Lubetkin, S., The Fundamentals of Bubble Evolution. *Chemical Society Reviews* **1995,** *24* (4), 243-250.
160. Cui, Z.; Takoudis, C. G., Initial Oxidation of H-Terminated Si (100) in O_3 (950 ppm)/O_2 and Pure O_2. *Journal of The Electrochemical Society* **2003,** *150* (11), G694.
161. Esposito, D. V.; Lee, Y.; Yoon, H.; Haney, P. M.; Labrador, N. Y.; Moffat, T. P.; Talin, A. A.; Szalai, V. A., Deconvoluting the Influences of 3d Structure on the Performance of Photoelectrodes for Solar-Driven Water Splitting. *Sustainable Energy & Fuels* **2017,** *1* (1), 154-173.
162. Leistra, J. A.; Sides, P. J., Voltage Components at Gas Evolving Electrodes. *Journal of The Electrochemical Society* **1987,** *134* (10), 2442-2446.
163. van der Linde, P.; Peñas-López, P.; Soto, Á. M.; van der Meer, D.; Lohse, D.; Gardeniers, H.; Rivas, D. F., Gas Bubble Evolution on Microstructured Silicon Substrates. *Energy & Environmental Science* **2018,** *11* (12), 3452-3462.
164. Kingsbury, D. L.; Marston, P. L., Mie Scattering near the Critical Angle of Bubbles in Water. *JOSA* **1981,** *71* (3), 358-361.
165. Warren, E. L.; Boettcher, S. W.; Walter, M. G.; Atwater, H. A.; Lewis, N. S., pH-Independent, 520 mV Open-Circuit Voltages of Si/Methyl Viologen$^{2+/+}$ Contacts through Use of Radial N+ P-Si Junction Microwire Array Photoelectrodes. *The Journal of Physical Chemistry C* **2011,** *115* (2), 594-598.
166. Fortune, W.; Mellon, M., Determination of Iron with O-Phenanthroline: A Spectrophotometric Study. *Industrial & Engineering Chemistry Analytical Edition* **1938,** *10* (2), 60-64.